Facet-Selective Growth on Nanowires Yields Multi-Component Nanostructures and Photonic Devices

Citation	Kempa, Thomas J., Sun-Kyung Kim, Robert W. Day, Hong-Gyu Park, Daniel G. Nocera, and Charles M. Lieber. 2013. "Facet-Selective Growth on Nanowires Yields Multi-Component Nanostructures and Photonic Devices." Journal of the American Chemical Society 135 (49) (December 11): 18354–18357. doi:10.1021/ja411050r.
Published Version	doi:10.1021/ja411050r
Accessed	February 17, 2015 4:59:21 AM EST
Citable Link	http://nrs.harvard.edu/urn-3:HUL.InstRepos:13364826
Terms of Use	This article was downloaded from Harvard University's DASH repository, and is made available under the terms and conditions applicable to Open Access Policy Articles, as set forth at http://nrs.harvard.edu/urn-3:HUL.InstRepos:dash.current.terms-of-use#OAP

(Article begins on next page)

Facet-Selective Growth on Nanowires Yields Multi-Component Nanostructures and Photonic Devices

Thomas J. Kempa,[†] Sun-Kyung Kim,[†,◊] Robert W. Day,[†] Hong-Gyu Park,*[§] Daniel G. Nocera,*[†] and Charles M. Lieber*[†,‡]

[†]Department of Chemistry and Chemical Biology and [‡]School of Engineering and Applied Sciences, Harvard University, Cambridge, Massachusetts 02138. [◊]Department of Applied Physics, Kyung Hee University, Gyeonggi-do, Republic of Korea. [§]Department of Physics, Korea University, Seoul 136-701, Republic of Korea.

Supporting Information Placeholder

ABSTRACT: Enhanced synthetic control of the morphology, crystal structure, and composition of nanostructures can drive advances in nanoscale devices. Axial and radial semiconductor nanowires are examples of nanostructures with one and two structural degrees of freedom, respectively, and their synthetically tuned and modulated properties have led to advances in nanotransistor, nanophotonic, and thermoelectric devices. Similarly, developing methods that allow for synthetic control of greater than two degrees of freedom could enable new opportunities for functional nanostructures. Here we demonstrate the first regioselective nanowire shell synthesis in studies of Ge and Si growth on faceted Si nanowire surfaces. The selectively deposited Ge is crystalline and its facet position can be synthetically controlled *in situ*. We use this synthesis to prepare electrically-addressable nanocavities into which solution soluble species such as Au nanoparticles can be incorporated. The method furnishes multi-component nanostructures with unique photonic properties and presents a more sophisticated nanodevice platform for future applications in catalysis and photodetection.

Semiconductor nanowires (NWs) represent a diverse class of nanomaterials whose synthetically-tunable structural, electronic, and optical properties[1–3] have enabled active nanodevices including high-performance field-effect transistors,[4] ultra-sensitive biological probes,[5–7] and solar cells and photonic devices with tunable optical spectra.[8–12] NWs can be classified according to the number of degrees of freedom (DoF) they possess, which represent fundamental physical coordinates along which their structure can be manipulated. Axial and radial (core/shell) modulated NWs have 1 and 2 DoF, respectively, and have been extensively studied and characterized.[2,13–19] Nevertheless, the properties of nanostructures possessing greater complexity and anisotropy have not been determined.

A nanostructure with 3 DoF and higher can be realized by breaking the rotational symmetry of conventional radial shell growth (Figure 1A). A high-resolution scanning electron micrograph (SEM) of a faceted core/shell Si NW (Figure 1B) reveals well-defined surfaces that were previously indexed[9] as {111}, {011}, and {113}. NWs with this same morphology and set of surface facets serve as the faceted templates from which all subsequent nanostructures in this study are grown. Following chemical vapor deposition (CVD) synthesis of the SiNW templates,[9] introduction of GeH_4 and H_2 at lower tem-
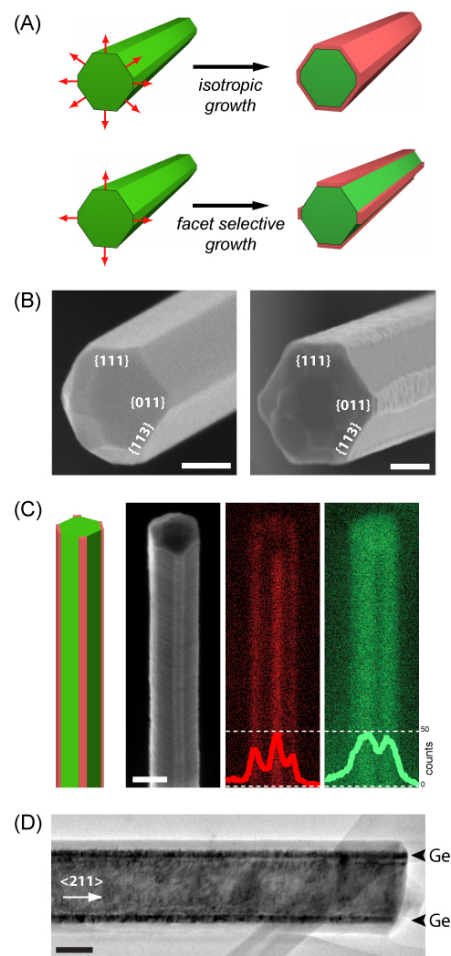

Figure 1. (A) Schematics depicting isotropic (top) versus anisotropic (bottom) growth of Ge (red) on a faceted Si template (green). (B) SEM of faceted Si template (left) and of nanostructure (right) after selective deposition of 10 nm of Ge (lighter contrast) on Si {111} and {011} surfaces. Images are oriented with {111} surfaces on top and bottom. Scale bars, 100 nm. (C) Schematic and SEM of a single nanostructure. Ge (red) and Si (green) EDS elemental maps of the same nanostructure and line profiles extracted from signal counts along the x-axis of the images. Images are oriented with {011} surface facing the reader. Scale bar, 200 nm. (D) Bright-field planview TEM of nanostructure. Scale bar, 100 nm.
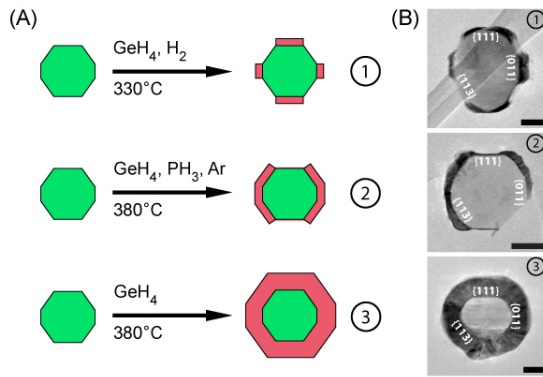
Figure 2. (A) Schematics summarizing three syntheses conducted to explore control of facet selective growth of Ge (red) on a faceted Si template (green). (B) Bright-field TEMs of 40 nm thick cross-sections of nanostructures **1–3** prepared according to the syntheses outlined in (A). Images are oriented with {111} surfaces on top and bottom. Scale bars, 50 nm.

perature and pressure into the same reactor (Supporting Information) yields a new product featuring selective material deposition on the {111} and {011} Si surface facets (Figure 1B). Energy dispersive x-ray spectroscopy (EDS) performed on the nanostructure (Figure 1C) confirms the elemental identity of the deposited material as Ge and reveals that facet selectivity is preserved along the length of the nanostructure. A planview transmission electron micrograph (TEM) of the anisotropic Si-Ge nanostructure (Figure 1D) reveals mesas with a uniform dark contrast corresponding to Ge. The Ge appears smooth and ordered and extends uniformly along the length of the {011} facet to which it is bound. Notably, these results differ significantly from the disordered, island morphologies that typify Stranski-Krastanov growth of Ge on planar and nanoscale Si surfaces.[20–23]

We performed syntheses using different Si templates, temperatures, and gas-phase species to determine their role in growth of Si-Ge (heteroepitaxial) and Si-Si (homoepitaxial) nanostructures with distinct anisotropies. After performing each synthesis for 5 min (Figure 2A, Figures S1 and S2), we prepared 40 nm thick cross-sections of the synthesized nanostructures and analyzed their morphology by bright-field TEM (Figure 2B, Figures S1 and S2).

TEM analysis of a nanostructure synthesized at 330 ˚C with GeH$_4$ and H$_2$ reveals dark contrast corresponding to Ge that has selectively grown on the {111} and {011} surfaces of the template (Figure 2: structure **1**). No dark contrast is visible on the {113} Si surfaces, thus reinforcing our previous contention of high selectivity for this Ge growth (Figure 1). Some variation in the Si morphology reflects both natural dispersion and TEM sample preparation (Figure S3 and Supporting Information). From TEM measurements and Ge growth time, we estimate the growth rates of Ge on {011} and {111} surfaces to be 2 nm/min and 1 nm/min, respectively. Repeating this synthesis in the presence of the faceted Si template coated with a 3 nm thick amorphous Si layer yields a thin isotropic Ge shell (Figure S1). Interestingly, growth at 650 ˚C with SiH$_4$ and H$_2$ leads to selective Si growth on the {111} surfaces of the Si template (Figure S2). This result is in contradistinction to the isotropic nanocrystalline Si shell[24] observed when this synthesis is performed on an axial Si NW without well-defined surface facets. Together, these results demonstrate that

the surface properties of the template play a vital role in enabling and controlling facet selective growth.

To determine whether Ge can be selectively grown on other facets, we examined syntheses at higher temperature and with various gas-phase precursors. TEM analysis of a nanostructure synthesized at 380 ˚C with GeH$_4$, PH$_3$, and Ar reveals (Figure 2, structure **2**) estimated Ge growth rates on the {113}, {011}, and {111} surfaces of 3.0, 1.6, and 0.3 nm/min, respectively. In structure **2**, a ×10 faster growth rate of Ge on {113} versus {111} is a striking reversal of the observed growth trend on these surfaces for structure **1**. We determined that Ar alone enhances growth of Ge on {113} versus {111} whereas PH$_3$ improves selectivity by suppressing Ge growth on the {111} surface, likely through passivation of Si surface sites with adsorbed phosphine or phosphine-derived species.[10,25] Finally, TEM analysis of a nanostructure synthesized at 380 ˚C with GeH$_4$ and no other gas-phase species reveals (Figure 2: structure **3**) an isotropic Ge shell and an estimated growth rate for this shell of 10 nm/min. This result confirms the importance of gas-phase species in mediating facet selective growth of Ge at higher temperatures. The yields of structures **1–3** determined from random sampling are in the range of 70–90%. In summary, these results represent the first gas-phase facet selective growth of Ge and Si on Si nanowire surfaces and establish that their facet position can be synthetically controlled *in situ* to elaborate unique nanostructures with higher anisotropy.

To explore more complex and opto-electronically active nanostructures we encapsulated nanoscale Ge regions within a Si *p-n* interface. The targeted architecture includes a faceted template with *p*-type and intrinsic Si shells, facet selective grown Ge, and finally a conformal shell of *n*-type Si (Figure 3A, Supporting Information). Notably, all synthetic steps were carried out in a continuous sequence in a single reactor for this complex structure. Bright-field TEM (Figure 3B) and EDS (Figure 3C,Figure S4) elemental mapping of the nanostructure cross-section verify that Ge was selectively embedded within the nanostructure while preserving the radial Si *p-n* junction. High-resolution TEM analysis of a region of the cross-section near the Si {111} interface (Figure 3D) reveals several important features. First, crystal lattice fringes proceed through the intrinsic Si/Ge/*n*-type Si regions of interest and terminate at the amorphous SiO$_x$ layer passivating the nanostructure. Second, two-dimensional Fourier transforms (Figure 3D) of lattice resolved TEM images from the intrinsic Si and Ge regions show well resolved spots that are consistent with the [211] zone-axis of the cubic crystal lattice.[26] Third, the sharp contrast changes visible in bright-field (Figure 3D) and dark-field TEM (Figure S4 inset) depict the abrupt interfaces formed between Si and Ge. In addition, high resolution TEM of a region of the cross-section near the Si {113} interface (Figure 3E) reveals an apparently clean intrinsic Si/*n*-type Si interface. Together, these results verify that the facet selective growth of Ge and subsequent conformal growth of *n*-type Si are crystalline and that clean, atomically-sharp interfaces can be designed and realized in these complex nanostructures.

High-resolution TEM analysis of a region of the cross-section near the Si {011} interface (Figure 3F and Figure S5) reveals several unique features. First, Si {111} lattice fringes progress across the intrinsic Si/Ge junction and are distorted near the edge of the Ge mesa where the Si {011} and {113} surfaces meet (Figure 3F). Second, a TEM spanning the full width of this region (Figure S5) shows a region of crystalline Ge that is 15 nm wide. Growth of planar Ge films on Si typi-
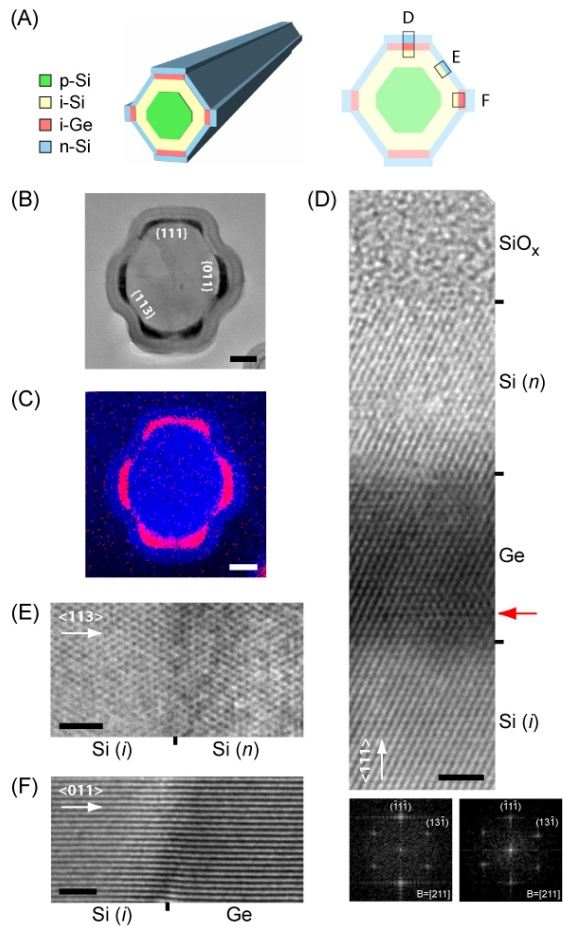
Figure 3. (A) Schematic (left) depicting a complex nanostructure with Ge regions selectively embedded within a *p*-i-*n* junction. Schematic (right) of the nanostructure cross-section with labels D, E, F corresponding to the figure panels where these interfaces are presented in detail. (B) Bright-field TEM of a 40 nm thick cross-section of the active nanostructure. Image is oriented with {111} surfaces on top and bottom. Scale bar, 50 nm. (C) EDS elemental map of section shown in (B) revealing Ge (red) embedded in Si (blue). Scale bar, 50 nm. (D) High-resolution TEM of the intrinsic Si/Ge/*n*-type Si region near the {111} interface within the nanostructure. The {111} plane lies parallel to the x-axis of the image. Two-dimensional FFTs of lattice-resolved TEMs of intrinsic Si (left) and Ge (right) regions. The cross-section is perpendicular to the nanostructure [211] zone axis. Red arrow indicates site of misfit dislocation. Scale bar, 2 nm. (E) High-resolution TEM of the intrinsic Si/*n*-type Si region near the {113} interface within the nanostructure. The {113} plane lies parallel to the y-axis of the image. Scale bar, 2 nm. (F) High-resolution TEM of the intrinsic Si/Ge region near the {011} interface within the nanostructure. The {011} plane lies parallel to the y-axis of the image. Scale bar, 2 nm.

cally proceeds by the Stranski-Krastanov mechanism.[20] An initial stage of epitaxial growth for thicknesses <5 nm[20] is followed by a disordered, three-dimensional (island) phase as strain energy increases due to the 4.2% Ge-Si lattice mismatch. Notably, our results demonstrate epitaxial Ge growth over greater thicknesses and suggest this is due to homogeneous relaxation of compressive strain[27,28] in the {011} plane, facilitated by the absence of crowding species on the adjacent {113} surface. Likewise, epitaxial growth of Ge persists for
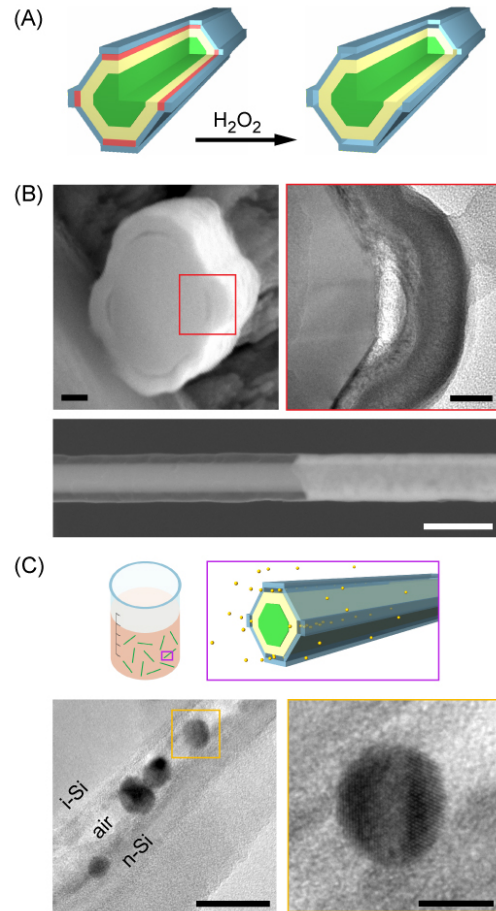

Figure 4. (A) Schematic demonstrating selective etching of Ge in H_2O_2 to form nanocavities. (B) SEM (left, scale bar, 50 nm) of the end of an etched nanostructure; high-resolution TEM (right, scale bar, 20 nm) of a cross-section near the {011} interface. Planview SEM (bottom, scale bar, 500 nm) of an etched nanostructure. (C) Schematic showing immersion of etched nanostructure in Au colloid solution. TEM image (left, scale bar, 20 nm) showing 4 Au nanoparticles infiltrated into the nanostructure cavity. High-resolution TEM image (right, scale bar, 5 nm) showing magnified view of a 7 nm Au nanoparticle.

growth in the <111> direction and shows evidence of formation of misfit dislocations[27,28] ~4 epilayers distant from the intrinsic Si/Ge interface (Figure 3D). The properties of the localized Si-Ge heterostructure regions and/or the role of Ge as a sensitizer within the nanostructure will be of future interest.

As a first step towards examining the optoelectronic properties of nanostructures with newly accessible anisotropies, we prepared a novel nanostructure with functional nanocavities. Specifically, hydrogen peroxide was used to etch Ge selectively and thus convert the nanostructure synthesized in Figure 3 to one with controlled nanocavities embedded within the *p-n* junction (Figure 4A, Supporting Information). SEM and TEM analyses (Figure 4B) verify that well-defined nanoscale cavities were etched in place of the Ge and that they extend uniformly along the lengths of the facet, where longitudinal etch distance is a function of the H_2O_2 etch time. Next, we fabricated single nanodevices with either a 10 or 20 nm wide nanocavity. Experimental and simulated external quantum

efficiency (EQE) spectra (Figure S6) obtained for the single nanodevices highlight several new features. An absorption centered at 500 nm (Figure S6A: peak 1) increases in amplitude as nanocavity size is enlarged from 10 to 20 nm. This enhanced absorption is well reproduced by simulation (Figure S6B: peak 1) and attributed to an increase in optical feedback (Figure S6C) due to change of refractive index[29,30] within the porous nanostructure. In addition, a very weak absorption at 625 nm blue shifts by 40 nm and its amplitude increases by a factor of 2.0 as nanocavity size is increased by 10 nm (Figure S6A: peak 2). Simulation shows reasonable agreement with this trend, predicting a 30 nm blue shift and 2-fold increase in amplitude for the same nanocavity size change (Figure S6B: peak 2). Analysis of simulated absorption mode profiles ascribes the wavelength shift to mode-pulling (Figure S6C) towards the lower refractive index air-filled nanocavity.[29,30] Notably, additional simulation results indicate that the spectral properties of these nanostructures can be significantly altered through subtle modification of the size and position of the internal nanocavities.

Nanoscale species may be delivered into the NW nanocavities. Immersion of the nanoporous structure in a 5 nm Au colloid solution led to infiltration of Au nanoparticles into the nanocavities (Figure 4C). A planview TEM of the nanostructure following immersion shows 4 Au nanoparticles trapped within a nanocavity (Figure 4C) that is encapsulated by intrinsic and n-type Si. This approach should be general for both metal and semiconductor nanoparticles as well as molecular dyes, thus opening up a new avenue for study of photosensitization and catalysis in unique electrically-addressable nanocavities. A nanostructure-catalyst framework presents a unique nanoporous scaffold within which to self-assemble catalysts; such a motif is appealing for the assembly of catalysts employed in energy conversion.[31] In addition, we expect our approach can accomplish facet selective synthesis of III/V or II/VI semiconductor NW materials, and nanoporous NW structures of these materials, that will be interesting targets of future study.

ASSOCIATED CONTENT

Supporting Information. Detailed description of synthetic methods, sample preparation, and device fabrication; Supplementary Figures S1–S5; additional references. This material is available free of charge via the Internet at http://pubs.acs.org.

AUTHOR INFORMATION

Corresponding Authors

hgpark@korea.ac.kr; dnocera@fas.harvard.edu; cml@cmliris.harvard.edu

Notes

The authors declare no competing financial interest.

REFERENCES

(1) Lu, W.; Lieber, C. M. *Nat. Mater.* **2007**, *6*, 841–850.
(2) Lu, W.; Lieber, C. M. *J. Phys. D: Appl. Phys.* **2006**, *39*, 387–406.
(3) Xia, Y.; Yang, P.; Sun, Y.; Wu, Y.; Mayers, B.; Gates, B.; Yin, Y.; Kim, F.; Yan, H. *Adv. Mater.* **2003**, *15*, 353–389.
(4) Xiang, J.; Lu, W.; Hu, Y.; Wu, Y.; Yan, H.; Lieber, C. M. *Nature* **2006**, *441*, 489–493.
(5) Patolsky, F.; Timko, B. P.; Zheng, G.; Lieber, C. M. *MRS Bull.* **2007**, *32*, 142–149.
(6) Tian, B.; Cohen-Karni, T.; Qing, Q.; Duan, X.; Xie, P.; Lieber, C. M. *Science* **2010**, *329*, 830–834.
(7) Cohen-Karni, T.; Timko, B. P.; Weiss, L. E.; Lieber, C. M. *Proc. Natl. Acad. Sci. USA* **2009**, *106*, 7309–7313.
(8) Tian, B.; Kempa, T. J.; Lieber, C. M. *Chem. Soc. Rev.* **2009**, *38*, 16–24.
(9) Kempa, T. J.; Cahoon, J. F.; Kim, S-K.; Day, R. W.; Bell, D. C.; Park, H-G.; Lieber, C. M. *Proc. Natl. Acad. Sci. USA* **2012**, *109*, 1407–1412.
(10) Kim, S-K.; Day, R. W.; Cahoon, J. F.; Kempa, T. J.; Song, K-Y.; Park, H-G.; Lieber, C. M. *Nano. Lett.* **2012**, *12*, 4971–4976.
(11) Cao, L.; White, J. S.; Park, J-S.; Schuller, J. A.; Clemens, B. M.; Brongersma, M. L. *Nat. Mater.* **2009**, *8*, 643–647.
(12) Kelzenberg, M. D.; Turner-Evans, D. B.; Kayes, B. M.; Filler, M. A.; Putnam, M. C.; Lewis, N. S.; Atwater, H. A. *Nano. Lett.* **2008**, *8*, 710–714.
(13) Kempa, T. J.; Tian, B.; Kim, D. R.; Hu, J.; Zheng, X.; Lieber, C. M. *Nano. Lett.* **2008**, *8*, 3456–3460.
(14) Tian, B.; Xie, P.; Kempa, T. J.; Bell, D. C.; Lieber, C. M. *Nat. Nanotechnol.* **2009**, *4*, 824–829.
(15) Qian, F.; Li, Y.; Gradecak, S.; Park, H-G.; Dong, Y.; Ding, Y.; Wang, Z. L.; Lieber, C. M. *Nat. Mater.* **2008**, *7*, 701–706.
(16) Caroff, P.; Dick, K. A.; Johansson, J.; Messing, M. E.; Deppert, K.; Samuelson, L. *Nat. Nanotechnol.* **2009**, *4*, 50–55.
(17) Wacaser, B. A.; Dick, K. A.; Johansson, J.; Borgstrom, M. T.; Deppert, K.; Samuelson, L. *Adv. Mater.* **2009**, *21*, 153–165.
(18) Schmidt, V.; Wittemann, J. V.; Gosele, U. *Chem. Rev.* **2010**, *110*, 361–388.
(19) Kodambaka, S.; Tersoff, J.; Reuter, M. C.; Ross, F. M. *Science* **2007**, *316*, 729–732.
(20) Eaglesham, D. J.; Cerullo, M. *Phys. Rev. Lett.* **1990**, *64*, 1943–1946.
(21) Kwon, S.; Chen, Z. C. Y.; Kim, J-H.; Xiang, J. *Nano. Lett.* **2012**, *12*, 4757–4762.
(22) Pan, L.; Lew, K-K.; Redwing, J. M.; Dickey, E. C. *Nano. Lett.* **2005**, *5*, 1081–1085.
(23) Ben-Ishai, M.; Patolsky, F. *Adv. Mater.* **2010**, *22*, 902–906.
(24) Tian, B.; Zheng, X.; Kempa, T. J.; Fang, Y.; Yu, N.; Yu, G.; Huang, J.; Lieber, C. M. *Nature* **2007**, *449*, 885–890.
(25) Cho, B.; Bareno, J.; Foo, Y. L.; Hong, S.; Spila, T.; Petrov, I.; Greene, J. E. *J. Appl. Phys.* **2008**, *103*, 123530:1–10.
(26) Wang, Z. L.; Kang, Z. C. *Functional and smart materials: Structural evolution and structure analysis*; Plenum Press: New York, 1998.
(27) Mullner, P.; Gao, H.; Ozkan, C. S. *Philos. Mag. A* **1997**, *75*, 925–938.
(28) Luth, H. *Solid Surfaces, Interfaces, and Thin Films* ed. 3; Springer: New York, 2001.
(29) Hecht, E. *Optics* ed. 4; Addison-Wesley: New York, 2002.
(30) Almeida, V. R.; Xu, Q.; Barrios, C. A.; Lipson, M. *Opt. Lett.* **2004**, *29*, 1209–1211.
(31) Surendranath, Y.; Lutterman, D. A.; Liu, Y.; Nocera, D. G. *J. Am. Chem. Soc.* **2012**, *134*, 6326–6336.

Facet-selective growth of Ge on Si nanowires yields multi-component nanostructures and photonic devices.
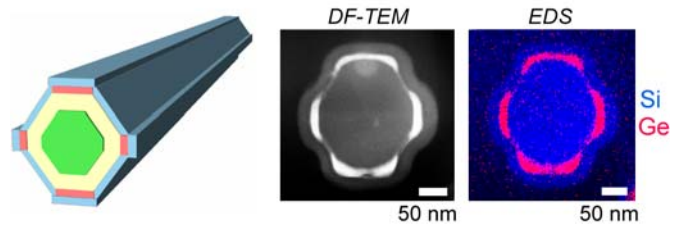
Supplementary Information

Facet-Selective Growth on Nanowires Yields Multi-Component Nanostructures and Photonic Devices

Thomas J. Kempa,[†] Sun-Kyung Kim,[†,◊] Robert W. Day,[†] Hong-Gyu Park,*[§] Daniel G. Nocera,*[†] and Charles M. Lieber*[†,‡]

[†]Department of Chemistry and Chemical Biology and [‡]School of Engineering and Applied Sciences, Harvard University, Cambridge, Massachusetts 02138. [◊]Department of Applied Physics, Kyung Hee University, Gyeonggi-do, Republic of Korea. [§]Department of Physics, Korea University, Seoul 136-701, Republic of Korea.

email: cml@cmliris.harvard.edu

Materials and Methods

Nanowire Syntheses

Si Nanowire (NW) Template. Au catalysts (100 nm diameter) were dispersed on poly-L-lysine functionalized 600 nm SiO_2-on-Si wafers. Substrates were inserted into a home-built quartz-tube reactor and the system was evacuated to 2.8 mTorr base pressure. Crystalline intrinsic Si nanowire (NW) cores were grown at 460 °C and 40 Torr for 1 h with flow rates of 1 and 60 standard cubic centimeters per minute (sccm) for silane (SiH_4), and hydrogen (H_2, Semiconductor Grade), respectively. A crystalline intrinsic Si shell was grown over these cores at 775 °C and 25 Torr for 30 min with flow rates of 0.15 and 60 sccm for silane and hydrogen, respectively.[1] A calibrated shell growth rate of 1.7 nm/min was determined from independent studies of shell thickness vs. growth time.

*Structure **1**.* Immediately following synthesis of the **Si NW template**, the reactor was purged to base pressure and re-pressurized to 4 Torr with a hydrogen flow rate of 20 sccm. This step was completed within 10 s. While pressurized, the reactor was cooled from 775 °C to 200 °C over 15 min. Once the reactor cooled to be sure that the sample was below the final Ge growth temperature, the furnace lid was closed and its heater turned back on. The Ge growth temperature set point (330°C) was reached within 3 min. Facet selective synthesis of Ge was carried out at 330°C and 5.8 Torr for 5 min with flow rates of 10 and 20 sccm for germane (GeH_4, 10% in H_2) and hydrogen, respectively.

*Structure **2**.* Immediately following synthesis of the **Si NW template**, the reactor was purged to base pressure and argon (Ar, Semiconductor Grade) introduced at a flow rate of 20 sccm. With argon continuously flowing, the reactor was cooled from 775 °C to 300 °C over 5 min. Once the reactor cooled to be sure that the sample was below the final Ge growth temperature, the furnace lid was closed and its heater turned back on. The Ge growth temperature set point (380°C) was reached within 3 min. Facet selective synthesis of Ge was carried out at 380 °C and 10 Torr for 5 min with flow rates of 10, 10, and 20 sccm for germane, phosphine (PH_3, 1000 ppm in H_2) and argon, respectively.

*Structure **3**.* Immediately following synthesis of the **Si NW template**, the reactor was purged to base pressure and cooled under vacuum from 775 °C to 300 °C over 5 min. Once the reactor cooled to be sure that the sample was below the final Ge growth temperature, the furnace lid was closed and its heater turned back on. The Ge growth temperature set point (380°C) was reached within 3 min. Synthesis of a conformal Ge shell was carried out at 380 °C and 4 Torr for 5 min with a flow rate of 5 sccm for germane.

Structure in Fig. 3. Crystalline *p*-type Si NW cores were grown at 460 °C and 40 Torr for 1 h with flow rates of 1, 5 and 60 sccm for silane, diborane (100 ppm in H_2) and hydrogen,

[1] Kempa, T. J.; Cahoon, J. F.; Kim, S-K.; Day, R. W.; Bell, D. C.; Park, H-G.; Lieber, C. M. *Proc. Natl. Acad. Sci. USA* **2012**, *109*, 1407–1412.

respectively. A crystalline *p*-type Si shell was grown over these cores at 775 ℃ and 25 Torr for 5 min with flow rates of 0.15, 1.5 and 60 sccm for silane, diborane and hydrogen, respectively. Next a crystalline intrinsic Si shell was grown over these cores at 775 ℃ and 25 Torr for 15 min with flow rates of 0.15 and 60 sccm for silane and hydrogen, respectively. Immediately following this synthesis, the reactor was purged to base pressure and re-pressurized to 4 Torr with a hydrogen flow rate of 20 sccm. While pressurized, the reactor was cooled from 775 ℃ to 200 ℃ over 15 min. Once the reactor cooled, the furnace lid was closed and its heater turned back on. The Ge growth temperature set point (330℃) was reached within 3 min. Facet selective synthesis of Ge was carried out at 330 ℃ and 5.8 Torr for 7 min with flow rates of 10 and 20 sccm for germane and hydrogen, respectively. Next, the reactor was heated under vacuum to 550 ℃ and held at this temperature for 1 min. Synthesis of a conformal shell of *n*-type Si was carried out at 550 ℃ and 5 Torr for 1.5 min with flow rates of 2 and 10 sccm for silane and phosphine.

Structure in Fig. S1. Immediately following synthesis of the **Si NW template**, the reactor was purged to base pressure and cooled under vacuum from 775 ℃ to 400 ℃ over 4 min. Once the reactor cooled, the furnace lid was closed and its heater turned back on. The Si growth temperature set point (450℃) was reached within 3 min. Synthesis of a conformal amorphous Si layer was carried out at 450 ℃ and 5 Torr for 1 min with a flow rate of 2 sccm for silane. Next, the reactor was purged to base pressure, re-pressurized to 4 Torr with a hydrogen flow rate of 20 sccm, and cooled over 2 min to 200 ℃. Subsequent synthesis conditions were as for structure **1**.

Structure in Fig. S2. Immediately following synthesis of the **Si NW template**, the reactor was purged to base pressure and hydrogen introduced at a flow rate of 60 sccm. With hydrogen continuously flowing, the reactor was cooled from 775 ℃ to 650 ℃ over 10 min. Facet selective synthesis of Si was carried out at 650 ℃ and 25 Torr for 20 min with flow rates of 0.15 and 60 sccm for silane and hydrogen, respectively.

TEM and EDS Sample Preparation and Characterization

Cross-sections for TEM studies were prepared by embedding NW structures in epoxy (Epo-Tek 353ND, Epoxy Technology). Samples were degassed to remove air bubbles and cured for 12 h at 30 ℃ in a vacuum oven. A diamond knife (Ultra 35°, DiATOME) was used with a sectioning tool (Ultra Microtome, Leica) to cut ~40 – 60 nm thick sections from the cured epoxy slugs. We note that the embedded nanowires have a distribution of orientation with respect to the growth substrate. During microtoming, this will lead to cross-sections that are cut off the nanowire growth axis, and thus yield a cross-section morphology that can vary from that expected for the ideal perpendicular section (Figure S3). The samples were transferred to lacey carbon grids for TEM analysis (JEOL 2100, JEOL Ltd.). An aberration corrected scanning TEM (cs-STEM, Libra 200 MC, Carl Zeiss NTS) equipped with twin EDS detectors and drift correction was used for acquisition of the EDS elemental map and

spectrum shown in Figs. 3C and S3. These EDS data were acquired at 1024×800 resolution over 1 h using a 400 ms pixel dwell time and 1.2 nm spot size with beam energy of 200 kV. An SEM (Supra 55VP, Carl Zeiss NTS) equipped with EDS detector was used for acquisition of the EDS elemental maps shown in Fig. 1C. These EDS data were acquired at 512×400 resolution over 20 min using a 500 μs pixel dwell time with beam energy of 4 kV.

NW Nanostructure Device Fabrication

NW nanostructures were synthesized with 10 and 20 nm wide embedded Ge regions (*Structure in Fig. 3.*) and then covered with a 30 nm conformal layer of SiO_2 using plasma enhanced chemical vapor deposition (PECVD). These nanostructures were shear transferred from their growth substrates to Si_3N_4.[2] SU-8 2000.5 was spin-coated to a thickness of 500 nm over the device substrate, pre-baked (95 ℃), and electron beam lithography (EBL) was used to define SU-8 etch masks over a portion of the nanostructure. SU-8 was developed and cured for 10 min at 180 ℃. Subsequently, etching to the *p*-type Si core was accomplished in the following order: 5 sec in BHF (for removal of the outer SiO_2 shell), 10 sec in potassium hydroxide (KOH 38 vol.% in water) at 60 ℃, 10 s in hydrogen peroxide (30 vol.% in water) at 60 ℃, and 12 sec in potassium hydroxide at 60℃. To selectively etch Ge from[3] the nanostructure, the device substrate was immersed in hydrogen peroxide at 60 ℃ for 30 min. Lastly, EBL followed by thermal evaporation of 4 nm of Ti and 300 nm of Pd was performed to define ohmic contacts to the etched (*p*-type) core and un-etched (*n*-type) shell. For the demonstration shown in Fig. 4C, a water solution containing 5 nm Au nanoparticles (Ted Pella, Inc.) was dropped onto the surface of an epoxy plug and allowed to evaporate. This plug was previously embedded with the Ge-etched nanowire structures (Fig. 4B) whose ends were exposed at its surface. Longitudinal TEM cross-sections ~100 nm thick were prepared by microtoming this slug at a 70° angle.

Device EQE spectra

Polarization-resolved photocurrent spectra were obtained on a home-built optical setup1 utilizing a standard solar simulator (150 W, Newport Oriel) with AM 1.5G filter as illumination source, a spectrometer (SpectraPro 300i, Acton Research) with 1200 g/mm grating and blaze angle of 500 nm, and an uncoated Glan-Thompson calcite polarizer (10GT04, Newport). Illumination power was measured using a power meter and low-power Si photodetector (1918-C and 918D-UV-OD3, Newport). Power spectra were acquired from 300 to 900 nm in 5 nm increments through 1.0, 1.3, and 2.0 mm diameter circular apertures to verify uniformity and accuracy of the power density used to calculate absolute EQE values. Nanostructure device photocurrents for transverse-electric (TE) and

---

[2] Javey, A.; Nam, S. W.; Friedman, R. S.; Yan, H.; Lieber, C. M. *Nano Lett.* **2007**, *7*, 773−777.

[3] Williams, K. R.; Gupta, K.; Wasilik, M. *J. Microelectromech. S.* **2003**, *12*, 761−778.

transverse-magnetic (TM) polarizations were measured from 300 to 900 nm in 5 nm increments using a semiconductor parameter analyzer (4156C, Agilent Technologies). Absolute EQE spectra were calculated using the wavelength-dependent photocurrent data collected as described above and the projected area of the nanostructures, which was measured by SEM. The projected area of the nanostructure was taken to be the exposed area of the un-etched nanostructure when viewed perpendicular to the substrate plane and did not include the area covered by the 300 nm thick metal contacts.

FDTD calculations

The absorption cross section of the simulated nanostructures under illumination by a normally incident plane wave was obtained by integrating J·E at each grid point, where J and E are the polarization current density and electric field, respectively. The absorption cross section was integrated over one optical period, and the wavelength of incident light was scanned from 280 – 1000 nm in 5 nm increments. The absorption efficiency is the ratio of the nanostructure absorption cross section to its physical cross section. Lastly, EQE is calculated by multiplying the absorption efficiency by internal quantum efficiency (IQE), where IQE was assumed to be unity. The nanostructure was simulated as a volume element with hexagonal cross-section and a spatial resolution of $5/\sqrt{3}$, 5, and 5 nm for x, y and z, respectively, where y lies along the nanostructure axis and z lies along the propagation direction of the incident plane wave. The simulated nanostructures had diameters of 230 nm, with 0, 10, or 20 nm wide air-filled cavities positioned 20 nm from the Si surface. All simulations included the Si_3N_4 device substrate and conformal SiO_2 layer used in the experiment. Periodic boundary conditions were applied along the axis of the nanostructure. To ensure that a single nanostructure experiences an infinite plane wave, we implemented the total-field scattered-field (TFSF) method. Without this method, a single nanostructure would be simulated as a periodic array of nanostructures along the x-axis. The measured refractive index and extinction coefficient of single crystal silicon[4] over the wavelength range, 280 – 1000 nm, was incorporated into the FDTD simulation.

---

[4] Lide, D. R. *CRC Handbook of Chemistry and Physics: A Ready-reference Book of Chemical and Physical Data*; CRC Press: Boca Raton, 2008.
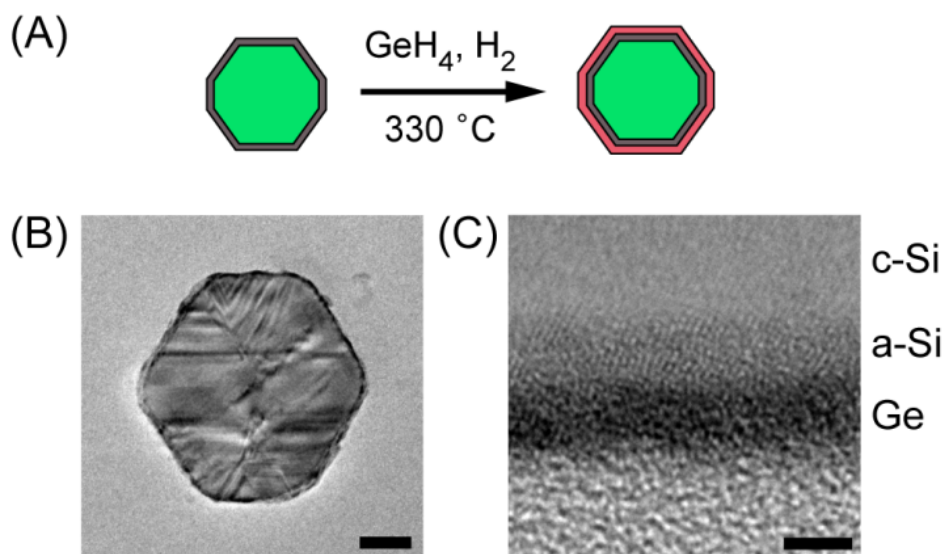
Figure S1. Role of template surface for facet selective growth of Ge. (A) Schematic of synthesis conditions which are identical to those for structure **1**. The Si template (green) has been covered with an amorphous Si shell (gray). (B) Bright-field TEM of a 40 nm thick cross-section of the nanostructure grown as outlined in (A). Image is oriented with {111} surfaces on top and bottom. Scale bar, 50 nm. (C) High-resolution TEM near {111} surface identifying the intentionally deposited amorphous Si shell and a thin conformal Ge shell. Scale bar, 3 nm.
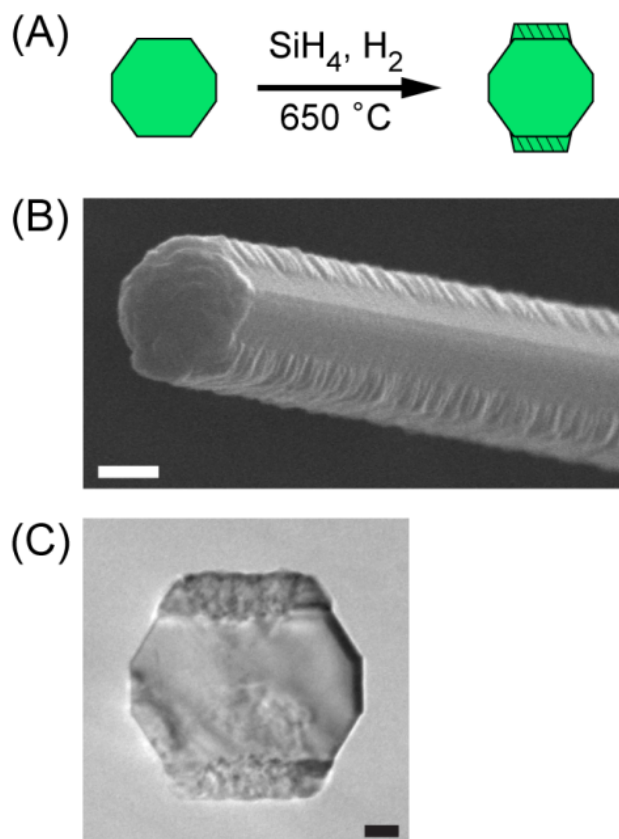
Figure S2. Facet selective Si homoepitaxial growth. (A) Schematic outlining synthesis conditions for facet-selective growth of Si on a Si template (green). (B) SEM of the nanostructure grown as outlined in (A). Image is oriented with {111} surfaces on top and bottom. Scale bar, 200 nm. (C) Bright-field TEM of nanostructure cross-section with {111} surfaces oriented on top and bottom of image. Scale bar, 50 nm. Facet-selective Si deposition is clearly visible on the {111} surfaces. By comparing the dimensions and facet lengths of the nanostructure against these same values for the template we confirmed that no Si grew on the {113} and {011} surfaces.
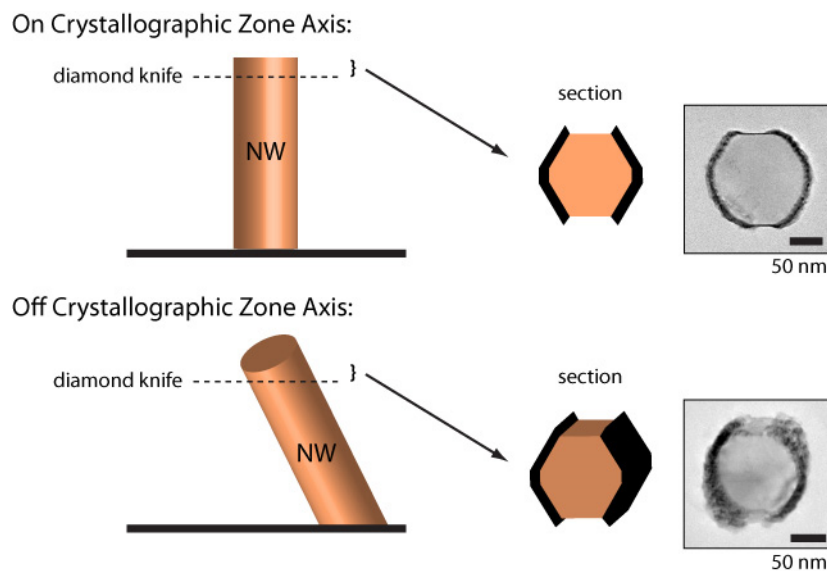
Figure S3. TEM cross-section preparation and images. As grown NWs have a range of orientations with respect to the growth substrate, and the sectioning plane of the diamond knife is parallel to the growth substrate for TEM cross-section sample preparation. In the ideal case, the diamond knife produces a section orthogonal to the NW's growth axis producing an undistorted axial slice when viewed in the TEM. In most cases, the diamond knife intercepts the NW at an angle off the nanowire axis thereby producing a distorted axial slice as observed in many TEM images. The upper and lower TEM images in the figure show ca. undistorted perpendicular and distorted off-axis cases, respectively.
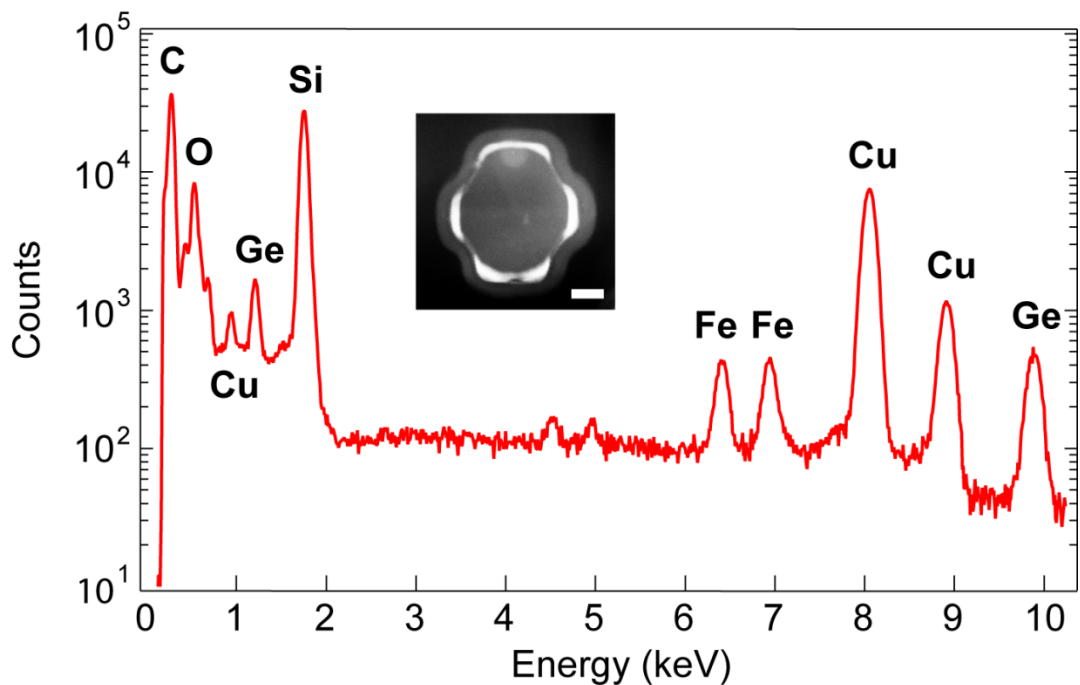
Figure S4. EDS spectrum of nanostructure with embedded Ge regions. EDS spectrum of a 40 nm thick cross-section (inset) of the nanostructure with Ge embedded within Si *p-n* junction. Ge Lβ (1.21 keV), Ge Kα (9.88 keV), and Si Kα (1.76 keV) lines are clearly discernable. Inset: dark-field TEM of the cross-section used to acquire the EDS spectrum. Scale bar, 50 nm.
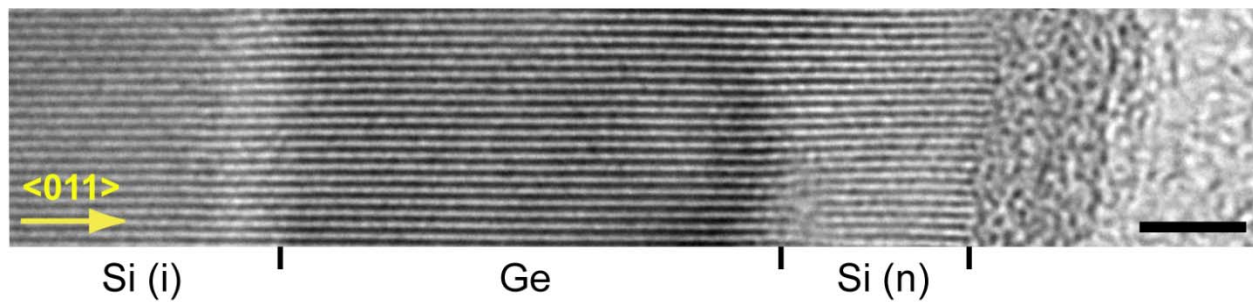
Figure S5. TEM of Si/Ge/Si interface near {011}. High-resolution TEM of the intrinsic Si/Ge/*n*-Si region near the {011} interface within the nanostructure. The {011} plane lies parallel to the y-axis of the image. Scale bar, 3 nm.
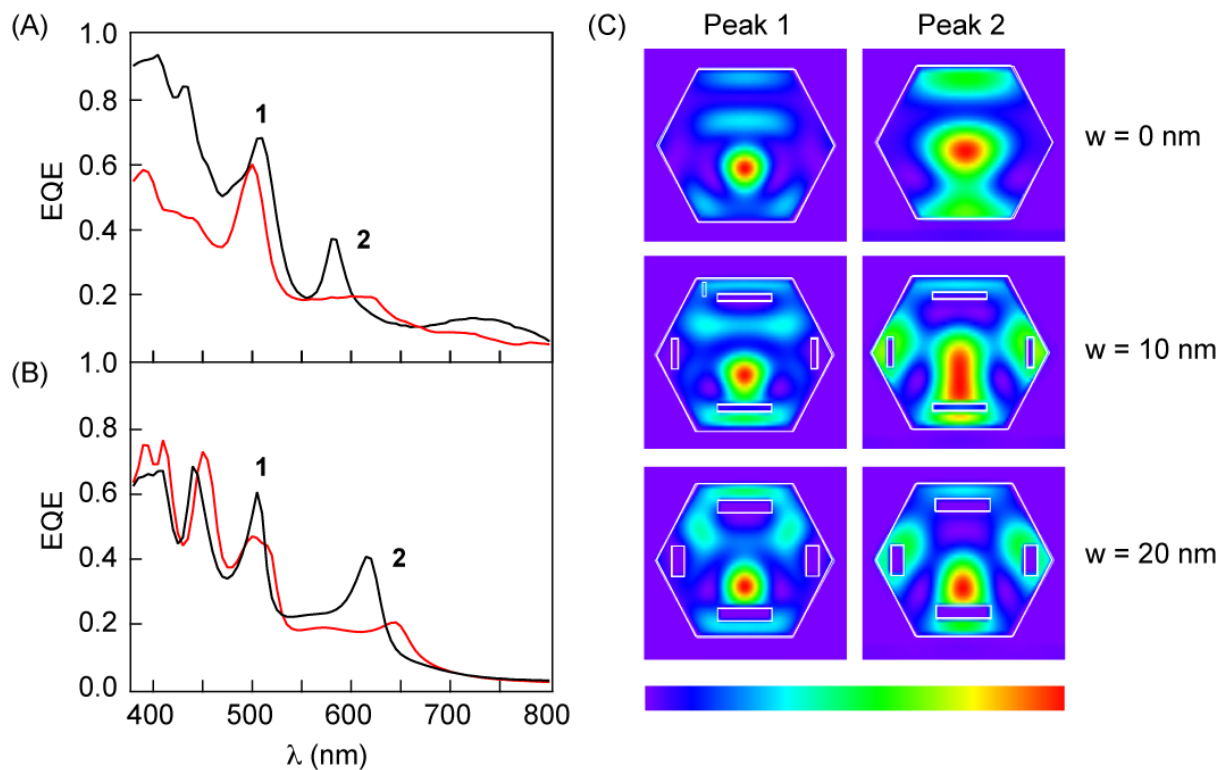
Figure S6. EQE spectra of NW devices containing nanocavities. (A) Experimental and simulated (B) absolute EQE spectra for the transverse-magnetic (TM) electric field polarization. Red and black lines correspond to nanostructures with 10 and 20 nm wide nanocavities, respectively. FDTD simulates nanostructures with hexagonal cross-sections, 230 nm diameters, and 10 and 20 nm wide cavities positioned 20 nm away from the outer Si surface of the nanostructure. SEM analyses of the devices used to obtain data in (A) show they have diameters of 224 and 236 nm. These values are within 2.6% of the simulated diameter. (C) Simulated absorption mode profiles for peak 1 (505 nm) and peak 2 (685, 645, and 615 nm) for cavity sizes of 0, 10, and 20 nm.